ADVANCED MATERIALS

www.advmat.de

Launching Phonon Polaritons by Natural Boron Nitride Wrinkles with Modifiable Dispersion by Dielectric Environments

*Jiahua Duan, Runkun Chen, Jingcheng Li, Kuijuan Jin, Zhigang Sun, and Jianing Chen**

Interference-free hyperbolic phonon polaritons (HPPs) excited by natural wrinkles in a hexagonal boron nitride (hBN) microcrystal are reported both experimentally and theoretically. Although their geometries are off-resonant with the excitation wavelength, the wrinkles compensate for the large momentum mismatch between photon and phonon polariton, and launch the HPPs without interference. The spatial feature of wrinkles is about 200 nm, which is an order of magnitude smaller than resonant metal antennas at the same excitation wavelength. Compared with phonon polaritons launched by an atomic force microscopy tip, the phonon polaritons launched by wrinkles are interference-free, independent of the launcher geometry, and exhibit a smaller damping rate ($\gamma \approx 0.028$). On the same hBN microcrystal, in situ nano-infrared imaging of HPPs launched by different mechanisms is performed. In addition, the dispersion of HPPs is modified by changing the dielectric environments of hBN crystals. The wavelength of HPPs is compressed twofold when the substrate is changed from SiO_2 to gold. The findings provide insights into the intrinsic properties of hBN-HPPs and demonstrate a new way to launch and control polaritons in van der Waals materials.

Polaritons[1,2] are collective excitations coming from coupling photons with quasiparticles such as plasmons or phonon. They confine free-space light to the nanoscale and thus provide a robust polaritonic probe to reveal new physics including electronic structure,[3] topological properties,[4,5] etc. In the ongoing demand for exploration of polaritons, hyperbolic media (HM),[6,7] whose axial and tangential components of dielectric tensor show opposite signs, support large-momentum hyperbolic polaritons (HPs) with much lower damping conditions than their evanescent counterparts (plasmon polaritons).[8–11] The unique properties of HPs in HM derive from the hyperboloid-type dispersion

$$k_z^2/\varepsilon_t + \left(k_x^2 + k_y^2\right)/\varepsilon_z = (\omega/c)^2 \quad (1)$$

Where $\varepsilon_t = \varepsilon_x = \varepsilon_y$ and ε_z are the tangential and axial permittivities, respectively. The solutions of Equation (1) are open hyperboloids of either type 1 ($\mathrm{Re}\varepsilon_z < 0$, $\mathrm{Re}\varepsilon_t > 0$) or type 2 ($\mathrm{Re}\varepsilon_z > 0$, $\mathrm{Re}\varepsilon_t < 0$), see **Figure 1**a,b. This hyperbolic dispersion gives rise to exotic behavior including directional propagation (both the Poynting vector S and the group velocity v_g have a fixed angle relative to the optical axis)[12–14] and negative phase velocity.[15] Compared with common media ($\mathrm{Re}\varepsilon_z > 0$, $\mathrm{Re}\varepsilon_x > 0$), HM show potential to extend conventional photonics in which the magnitude rather than direction of k is limited.

A major source of interest in HM was their experimental exploration in man-made hyperbolic metamaterial (HMM) structures, such as periodic metal nanostructures[16] or metal–dielectric multilayers.[7,17] However, the optical confinement and spatial resolution of HMMs are restricted because their maximum wavevector is limited by the size of the artificial unit cell, let alone losses in the constituent metals, and their complex nanofabrication. Recently, some research has identified[18,19] hexagonal boron nitride (hBN) as a low-loss natural HM capable of supporting hyperbolic phonon polaritons (HPPs), which breaks the upper limit on the propagating wavevector due to its atomic-scale unit cell. The polar bond between B and N makes hBN optically anisotropic, meaning that the dielectric responses in orthogonal directions (in-plane and out-of-plane) have opposite signs. As shown in Figure 1c, hBN gives two separate spectral bands called lower and upper Reststrahlen bands. The upper band spans ω = 1370–1600 cm^{-1}, where $\mathrm{Re}\varepsilon_t$ is negative while the $\mathrm{Re}\varepsilon_z$ is positive. In the lower band (ω = 760–820 cm^{-1}), signs of the components of the permittivity are reversed. Hence, the lower (upper) bands offer type 1

Dr. J. Duan, Dr. R. Chen, Dr. J. Li, Prof. K. Jin, Prof. J. Chen
Institute of Physics
Chinese Academy of Sciences
100190 Beijing, China
E-mail: jnchen@iphy.ac.cn

Dr. J. Duan, Dr. R. Chen, Dr.J. Li, Prof. K. Jin, Prof. J. Chen
School of Physical Sciences
University of Chinese Academy of Sciences
100049 Beijing, China

Prof. K. Jin, Prof. J. Chen
Collaborative Innovation Center of Quantum Matter
100190 Beijing, China

Prof. Z. Sun
Center for Theoretical and Computational Chemistry, and State Key Laboratory of Molecular Reaction Dynamics
Dalian Institute of Chemical Physics
Chinese Academy of Sciences
Dalian 116023, China

The ORCID identification number(s) for the author(s) of this article can be found under https://doi.org/10.1002/adma.201702494.

DOI: 10.1002/adma.201702494

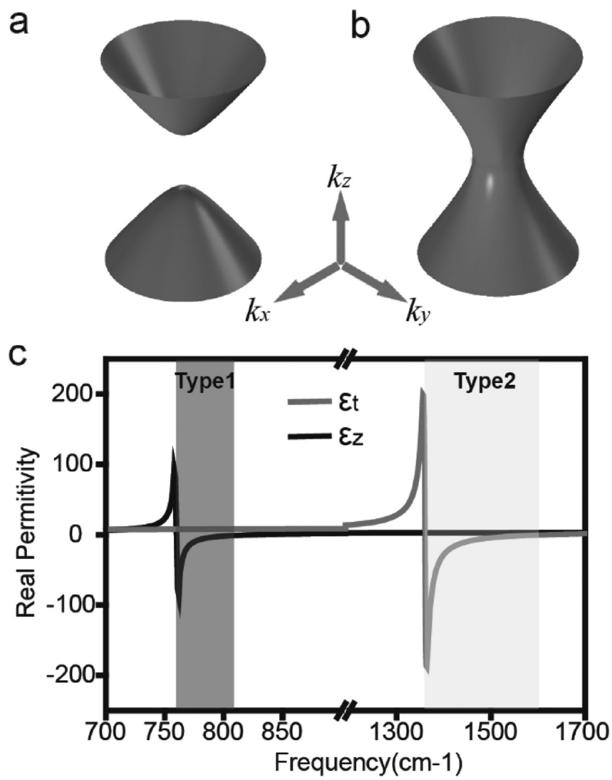

Figure 1. Hyperbolic behavior of the natural hBN. a) Schematic isofrequency surface for a type 1 hyperbolic media. b) Schematic isofrequency surface for a type 2 hyperbolic media. c) Real components of the permittivity tensor of hBN crystal (ε_t and ε_z represent the tangential and axial permittivities, respectively). The frequency of out-of-plane mode ($\omega_{TO} \approx 760$, $\omega_{LO} \approx 820$ cm^{-1}) and in-plane mode ($\omega_{TO} \approx 1370$, $\omega_{LO} \approx 1600$ cm^{-1}) of optical phonon are shown by vertical lines. The corresponding lower (type 1) and upper (type 2) Reststrahlen bands are shaded in grey.

(type 2) hyperbolic response, and make strongly confined HPPs in hBN, which are essential to many imaging, thermal, and quantum applications.[2] Recently, one burgeoning near-field technique named scattering-type scanning near-field optical microscopy (s-SNOM) realizes the real-space imaging and characterization of polaritons in van der Waals materials[8–11,18] and provides manifold novel insights in the study of polaritons inaccessible to far-field methods. In previous s-SNOM experiments, the metallic atomic force microscopy (AFM) tip must simultaneously play the roles of launcher and detector.[8–11,13,18] The tip-launched polariton waves propagate radially outward from the tip and reflect back upon reaching the defects, finally forming interference waves. This method-intrinsic interference decreases the quality factor of polaritons and produces complicated image analysis. Another bottleneck faced in hBN materials is the control of these HPPs, mostly because of settled crystal lattice of hBN and large momentum mismatch between polaritons and photonic modes of the same frequency. Due to the insulation (gate-tunable method is not possible), the wavelength of HPPs can be controlled only by a large number of repeated sample preparations to luckily single out ideal hBN thickness. Moreover, unlike well-studied graphene plasmons,[4,9,20,21] the influence of defects on HPPs in hBN has been elusive so far.

Here, we launch interference-free HPP wavefronts by exploiting natural wrinkles on hBN and tune the dispersion of HPPs by changing dielectric environment. In order to study the different excitation mechanisms, we first perform in situ nano-IR imaging of hBN-HPPs excited by different launchers (AFM tip/wrinkles/gold antennas). The ratio of distance between neighboring bright fringes measured from wrinkle-launched (λ_p) and tip-launched ($\lambda_p/2$) HPPs is always at two, regardless of the crystal thickness. We theoretically and experimentally demonstrate that natural wrinkles on hBN crystals serve as geometrically independent broadband antenna with advantages including nanoscale dimension (≈200 nm), interference-free wavefront, and low damping ($\gamma \approx 0.028$). On top of that, we provide the first experimental demonstration of HPP wavelength-control through changing the conventional SiO_2 substrate to a metal.

Figure 2 shows the numerical simulation of HPPs launched by wrinkles and gold antennas. The spatial dimensions of wrinkles and gold edge are tens of nanometers, and they therefore have a similar k spectrum to the conventional AFM tip[15] (a maximum momentum increment is about $1/a$,[22] where a is the curvature radius of the AFM tip), which provides a sufficiently high-momentum value to compensate for the momentum mismatch between photons and polaritons. With a plane-wave excitation source of $\lambda_0 = 12.66$ µm and $\lambda_0 = 6.45$ µm, we observed type 1 (Figure 2a,b) and type 2 (Figure 2e,f) HPPs parallel to the wrinkle and gold edge. The directional rays of HPPs, which propagate within the hBN slab and reflect from the bottom and top surfaces, can be described as a superposition of eigenmodes Mn (n = 0, 1, 2, 3...). Although the high-order modes have a higher Q factor, our simulation only shows the fundamental mode HPP-M0 due to the dramatically short wavelength and corresponding small propagating length of Mn ($n \geq 1$). In Figure 2a,e, the distance between the neighboring bright fringes directly gives the wavelength of type 1 and type 2 HPP-M0s launched by wrinkles, which are 289 and 367 nm, respectively. Accordingly, the 2D Fourier transformation (2D-FT) of Figure 2a,e yields bright dots located at $k_{HPP} = 2\pi/\lambda_{HPP} = 44k_0$ for type 1 and $18k_0$ for type 2 (Figure 2c,g), consistent with propagating HPPs. Here, the k_0 for type 1 and type 2 HPPs are 0.496 µm^{-1} ($2\pi/\lambda_{0\text{-type 1}}$) and 0.974 µm^{-1} ($2\pi/\lambda_{0\text{-type 2}}$), respectively. The momentum is distributed only along the k_x direction, which can be ascribed to the 1D nature of our wrinkles. It is also worth noting that a change of wrinkle geometry (such as height or shape) does not affect the wavelength of launching HPPs (Figures S1 and S2, Supporting Information), making wrinkles a geometrically independent nanoantenna, which is significant for future nanoscale polaritonic circuit and device development.

In order to further study the influence of dielectric environment, we encapsulate a gold antenna between the hBN crystal and SiO_2 substrate, differently from previous report where gold rods are fabricated on top of hBN.[15,23] Compared with wrinkle-launching, HPPs launched outside the gold film have the same wavelength (λ_p = 280.7 nm for type 1 in Figure 2b and λ_p = 367 nm for type 2 in Figure 2f, respectively), but exhibit different wavefronts that depend on the shape of the antenna. However, on top of the gold film, the HPPs are either loosed (λ_p = 525.5 nm) or compressed (λ_p = 185.6 nm) for type

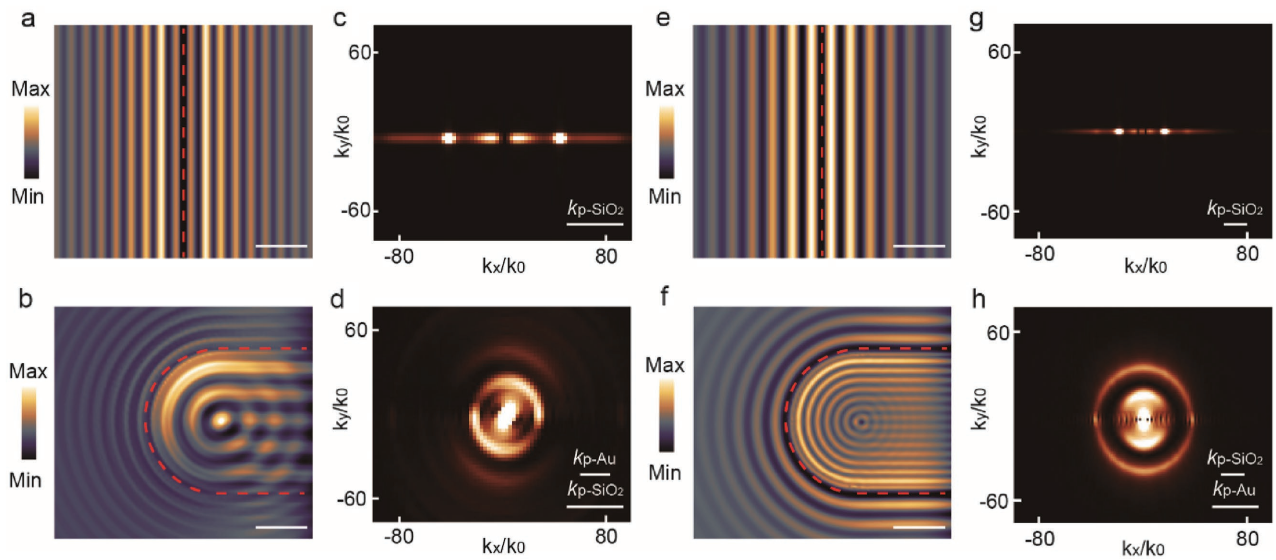

Figure 2. Numerical simulations of launching HPPs with wrinkles and metal antennas. a) Near-field distribution of 62.7 nm wrinkle on 77 nm hBN crystal on SiO_2 substrate. b) Near-field distribution of 77 nm hBN crystal with a micrometer-size gold antenna. The antenna is encapsulated between hBN and the SiO_2 substrate. The incident frequency in (a) and (b) is 790 cm^{-1}, which is located in lower Reststrahlen band. c,d) Absolute value of the Fourier transform of the near-field amplitude in (a) and (b), respectively. e,f) The launched type 2 HPPs in same hBN crystal as (a) and (b) except for different incident frequency of 1550 cm^{-1}, which is located in upper Reststrahlen band. g,h) Absolute value of the Fourier transform of the near-field amplitude in (e) and (f), respectively. The excitation method is plane-wave source and the scale bar is 1 μm. The red dashed lines show the position of wrinkle and the outline of gold antenna.

1 and type 2, compared with the same case on SiO_2 substrate (see more details in the Supporting Information). This opposite variation trend is explained by the inverse dispersion relation of type 1 and type 2 HPPs.[12,13] Thus, varying the dielectric environment offers an easy way to control the wavelength of HPPs in hBN microcrystal without changing the crystal thickness. Due to the 2D nature of the gold antenna, the 2D-FT of Figure 2b,f yields two bright rings of diameter k_p-Au and k_p-SiO_2, shown in Figure 2d,h. The k_p-SiO_2 are $44k_0$ and $18k_0$ for type 1 and type 2, respectively, which are the same as those for the HPPs launched by a wrinkle. However, the k_p-Au is reduced to $24k_0$ and increased to $35.9k_0$ for type 1 and type 2, consistent with HPPs propagating in hBN on top of gold film. The numerical simulations clearly show that both the wrinkle and metal antenna are able to launch HPPs, and that the wavelength of HPPs can be controlled by varying the dielectric environment.

For experimental demonstrations, we fabricate a sample of mechanically exfoliated hBN and image the electrical near-field distribution with s-SNOM.[8,9,21,24] Theoretically, we considered both type 1 and type 2 HPPs; experimentally, however, only the type 2 HPPs can be measured by a CW (continuous wave) laser source[12,14,25] due to the unavailability of lasers capable of producing light in the 760–820 cm^{-1} frequency range. In order to study the inherent properties of HPPs, it is preferred to avoid electron heating[26,27] by the pulses of the broadband source and choose CW laser source. Meanwhile, the out-of-plane mode (type 1) is much weaker than the in-plane mode (type 2) due to the nature of the hBN slab.[25] Therefore, we carried out discrete-frequency near-field imaging of type 2-HPPs by our monochromatic quantum cascade lasers (QCLs) with ω_0 = 1500–1600 cm^{-1}. In contrast to their counterpart surface polaritons,[20,21,26,28] the HPPs in hBN are volume modes and expected to be much less sensitive to surface defects.[15] The HPPs propagate inside the hBN and their back reflection at wrinkle or gold antenna is considered to be too weak to form interference with propagating HPPs. Hence, the AFM tip in our experiment just acts as a passive scatter rather than an HPP launcher. **Figure 3**a shows the mechanism of the experiment, which is fundamentally different with the previous works,[8,9,18] where half of HPP wavelength is measured due to the complex interference. The classical tip-excited HPP fringes are more closed ($\lambda_p/2$) and exist at the edge of the crystal (Figure S4, Supporting Information) where the back reflection coefficient is about 1.[15,18] As shown in Figure 3b, the ratio of distance between neighboring bright fringes measured from wrinkle-launched (λ_p) and tip-launched ($\lambda_p/2$) HPPs stays as a constant of 2, regardless of the thickness of hBN crystal. In the optical nanoimages, we normalized near-field amplitude $s(\omega) = s_4^0(\omega)/s_4^{Au}(\omega)$. Here, $s_4^0(\omega)$ and $s_4^{Au}(\omega)$ are the fourth-order demodulated harmonics of the near-field amplitude detected for hBN and Au standard reference sample, respectively. Figure 3c,i shows the topography of a 62.7 nm wrinkle on 77 nm hBN and a 90 nm wrinkle on 115 nm hBN, respectively. The line profiles for topography (Figure 3f,l) show that the width of the wrinkle is just about 200 nm, which is much smaller than classical resonant metal antennas.[15,24] There are three wrinkles with different heights (75, 62.7, and 21.9 nm) on the 77 nm thick hBN crystal (see more details in Figure S6 in the Supporting Information), which indicate that the existence of natural wrinkles on mechanically exfoliated hBN is very common. All three wrinkles are able to launch the same HPPs, consistent with our computational observation of geometrical independence (Figure S6, Supporting Information). With incident frequency of 1550 cm^{-1}, near-field images of the

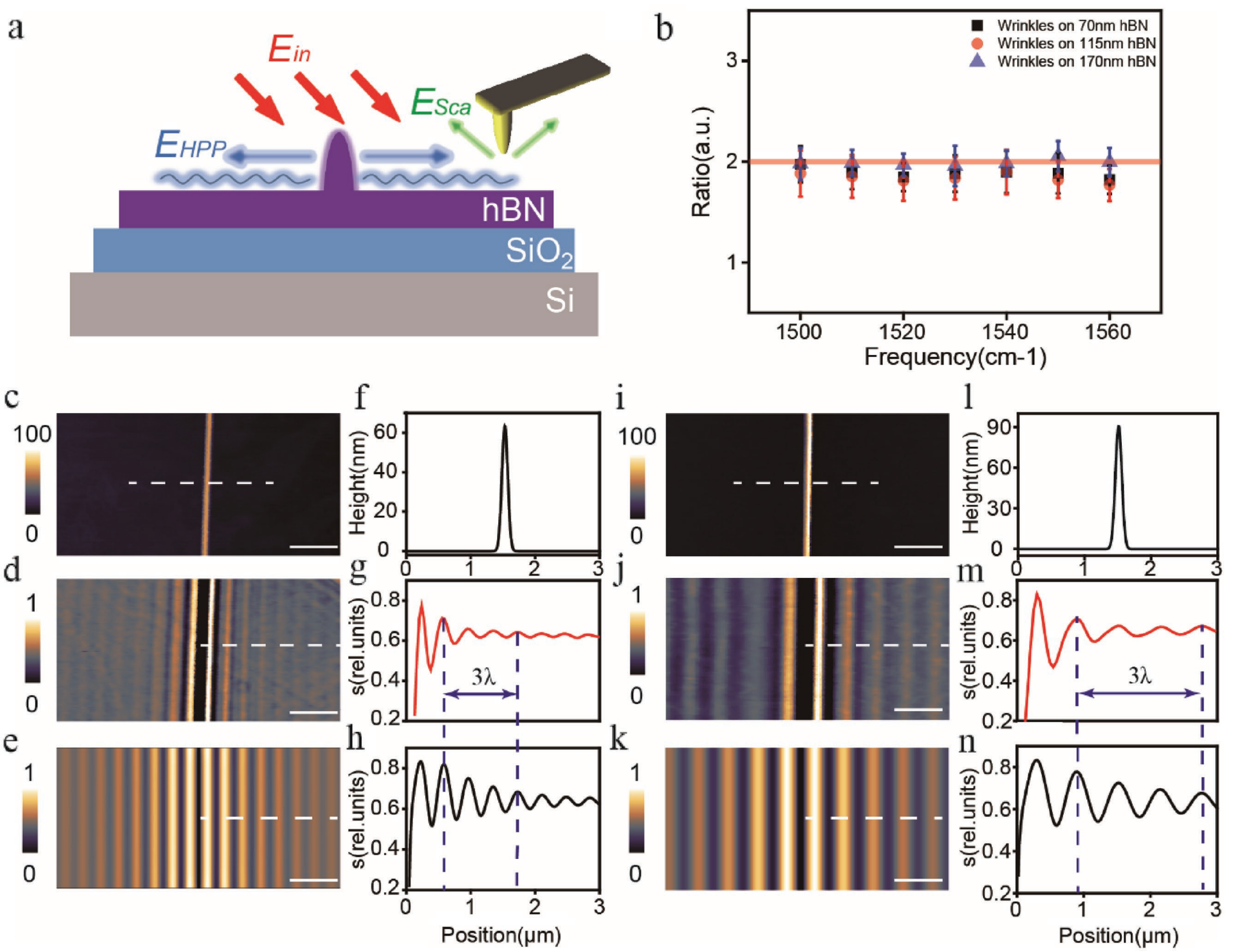

Figure 3. Experimental demonstration of a wrinkle-based HPP launcher. a) Schematic of our nano-IR imaging experiment. The wrinkle on hBN is illuminated with IR light to launch HPPs, which is probed through an AFM tip. b) The ratio between ensemble-averaged distances of adjacent bright fringe extracted from wrinkle and crystal edge on the same hBN slab. The error bars are the statistical standard deviations with different wrinkles on one hBN. c) Topography image of a 62.7 nm wrinkle on 77 nm hBN. d) The experimental infrared near-field image of the wrinkle shown in (c) with incident frequency of 1550 cm^{-1}. e) Corresponding numerical simulation of near-field distribution around wrinkle shown in (c). f–h) Line profiles along the dashed white line in (c)–(e), respectively. i) Topography image of a 90 nm wrinkle on 115 nm hBN. j) The experimental infrared near-field image of the wrinkle shown in (i) with incident frequency of 1550 cm^{-1}. k) Corresponding numerical simulation of near-field distribution around wrinkle shown in (i). l–n) Line profiles along the dashed white line in (i)–(k), respectively. All plasmonic line profiles are averaged over a width of 128 nm. Scale bar, 1 µm.

hBN slabs (Figure 3d,j) indicate that HPPs propagate perpendicular to the wrinkle. The nanoinfrared images show similar periods on both sides of the wrinkles. With the incident frequency of 1550 cm^{-1}, the deviation between left-side wavelength (λ_{left}) and right-side wavelength (λ_{right}) for 77 nm hBN and 115 nm hBN are only $\Delta \approx 4.3\%$ and $\Delta \approx 0.7\%$, respectively (more details are in Section S9 in the Supporting Information). As shown in Figure S15 (Supporting Information), the hBN-HPPs on the left and right sides have similar wavelength and dispersion when we change to different incident frequencies. It should be noticed that the first fringe on the left side of the wrinkle appears wider in Figure 3j. In Figure S16 (Supporting Information), we show two possible mechanisms behind this phenomenon, including different tip-wrinkle coupling and air influence. In order to avoid the influence from this difference, we exclude this fringe when we extract intrinsic HPP properties.

The wavelength becomes larger when the thickness of hBN increases, conforming to the linear scaling between wavelength and hBN thickness (Figure S4g, Supporting Information). The agreement between our experimental observations and numerical simulations (Figure 3e,k) under plane-wave excitation further indicate that the AFM tip acts as a detector rather than a launcher of HPPs. For quantitative comparison, we show experimental near-field amplitude line profiles in Figure 3g,m, with the corresponding simulated line profiles in Figure 3h,n. The wavelengths of wrinkle-launched HPPs on 77 nm hBN and 115 nm hBN are 366.7 and 619.3 nm, respectively. Both the oscillation periods and relative field strengths show excellent agreement between simulation and experimental results. Intriguingly, the wrinkle-launched HPPs propagate about ten polariton wavelengths (Figure S7, Supporting Information), which is longer than the tip-launched HPPs. The decay of propagating polaritons in 2D materials can be described by the following equation[10]

$$\xi_{\mathrm{opt}}(x) = A\frac{e^{i2qx}}{\sqrt{x}} + B\frac{e^{iqx}}{x} \tag{2}$$

Here, q is the wavevector of HPPs. The first term and second term of Equation (2) represent tip-launched standing wave and wrinkle-launched interference-free wave, respectively. Due to the domination of interference-free HPPs wave in our experiments, we neglect the first term and define the damping rate $\gamma = \mathrm{Im}(q)/\mathrm{Re}(q)$. More fitting details can be found in Section S8 in the Supporting Information. We find that the damping rate (γ) of wrinkle-launched HPPs is ≈0.028, which is much smaller than tip-launched HPPs ($\gamma \approx 0.07$) and graphene plasmons ($\gamma \approx 0.1$).[8,9] Although the intrinsic damping rate of the HPPs should be the same, regardless of whether they are tip-launched or wrinkle-launched polaritons, there is an additional loss channel of $1/\sqrt{r}$ with tip-launched HPPs due to their radial propagation[15] (r is the propagating distance). The experimental results show that natural wrinkles can be used as nanoantenna with much smaller sizes compared with resonant metal antennas to launch propagating HPPs with less loss.

In order to confine HPPs through varying the dielectric environment, we transferred the same 77-nm-thick hBN flake on top of the fabricated gold slab of 2.5 µm in diameter, which is incorporated into a SiO_2 substrate. The gold antenna is encapsulated between hBN and SiO_2 substrate, as shown in schematic **Figure 4**a. The hBN crystal remains flat as demonstrated by AFM. To simplify the analysis, we assume that the metallic antenna is buried into the SiO_2 which is reasonable due to the flat topography of hBN.[13] This metal antenna converts the incident electromagnetic field into a strongly confined near field at the gold edge, compensating for the momentum mismatch and launching the HPPs. The interpretation of the near-field image (Figure 4b) at ω_0 = 1530 cm^{-1} is straightforward: the gold-launched HPPs propagate outward from the gold edge and have similar properties as wrinkle-launched ones. The line profiles representing hBN on top of SiO_2 (white dashed line) and gold (red dashed line) substrates are shown in Figure 4c,d, respectively. The images show that the wavelength of HPPs is compressed from 505.8 to 236.0 nm when the substrate is changed from dielectric to metal. The experimental data agree well with numerical simulation (Figure 4e). The calculated near-field profiles along the dashed white and red lines in Figure 4e are displayed in Figure 4f,g, which quantitatively agree with the experimental ones. Since all the HPPs come from the same hBN crystal (77 nm), the distances between neighboring bright fringes extracted from wrinkle and gold antenna are the same, which are double that extracted from the hBN edge ($\lambda_{\mathrm{HPPs}} = \lambda_{\mathrm{wrinkle}} = \lambda_{\mathrm{gold}} = 2\lambda_{\mathrm{edge}}$). An intuitive way to indicate both the dispersion and the damping is through a false-color map of $\mathrm{Im}r_{\mathrm{p}}(q, \omega)$ at real q and ω. The $r_{\mathrm{p}}(q, \omega)$ can be calculated through the Fresnel equations

$$r_{\mathrm{p}}(q,\omega) = \frac{r_{\mathrm{a}} + r_{\mathrm{s}} e^{i2k_{\mathrm{e}}^{z}d}}{1 + r_{\mathrm{a}} r_{\mathrm{s}} e^{i2k_{\mathrm{e}}^{z}d}} \tag{3}$$

where the functions r_{a} and r_{s} are the reflectivity of the air/hBN and hBN/SiO_2 interfaces, d is the thickness of the hBN crystal, and k_{e}^{z} is the z-axis momentum of the "extraordinary ray" in hBN. The dispersion relation of HPPs in 77 nm hBN is shown in Figure 4h. For comparison, we plot the experimental data of wrinkle-launched (white cross), gold-launched (green cross), and tip-launched HPPs (blue dot). The wavelengths measured at the hBN edge are stretched by a factor of two to account for the interference of standing wave. All experimental data show quantitative agreement with the calculated principle branch of hyperbolic polaritons. In Figure 4i, the dispersion relation of hBN on top of gold film is shown in a false-color map, with hBN on SiO_2 as yellow dashed line for comparison. This further confirms that larger-momentum HPPs are launched through changing the dielectric environment around hBN. To the best of our knowledge, the near-field images here are the first experimental demonstration of controlling HPP wavelength through dielectric environment after being predicted by the recent review.[1]

Our nano-IR imaging experiments show that the intrinsic wrinkles on hBN can serve as an off-resonant antenna to launch wavefronts of HPPs. Since they are interference-free, the damping rate of wrinkle-launched HPPs is only about 0.028, which is much smaller than tip-launched HPPs ($\gamma \approx 0.07$) and graphene plasmon ($\gamma \approx 0.1$). Meanwhile, the dimension of wrinkles (≈200 nm) is one order of magnitude smaller than that of the corresponding resonant metal antennas (≈1 µm). The in situ infrared imaging of HPPs excited by different mechanisms reveals constant relationship (≈2) of oscillation period in interference ($\lambda_{\mathrm{p}}/2$) and interference-free condition (λ_{p}). By placing an hBN flake on different substrates, we observe different variation tendency of dispersion for type 1 and type 2 HPPs in our simulation. For the first time, we demonstrate experimentally that it is feasible to control HPP wavelength through changing the dielectric environment. Our findings are important for the future polaritonic circuits and devices.

Experimental Section

Sample Preparation and Transfer: Microcrystals of hBN were mechanically exfoliated from bulk samples and then transferred to 285-nm-thick SiO_2/Si substrate. The optical microscopy, AFM, and Raman spectroscopy were used to identify the hBN crystal. The exfoliated hBN slab on SiO_2/Si substrate was transferred through micromanipulation technique. The gold antenna was fabricated by ultraviolet lithography and encapsulated between hBN slab and SiO_2 substrate.

Infrared s-SNOM Measurements: The nanoimaging experiments in the main text and the Supporting Information were performed using a s-SNOM. The s-SNOM is a commercial system (Neaspec GmbH) equipped with QCLs (from Daylight Solutions). The incident frequency spanned from 1500 to 1600 cm^{-1}. The s-SNOM was based on an AFM operating in the tapping mode with $\Omega \approx 300$ kHz and an amplitude of ≈60 nm. A pseudoheterodyne interferometric method was applied to extract both the near-field amplitude and phase of HPPs in hBN. The near-field signal was demodulated at a fourth harmonic to suppress background scattering. The near-field amplitude $s_4(\omega) = s_4^0(\omega)/s_4^{\mathrm{Au}}(\omega)$ was normalized. Here, $s_4^0(\omega)$ and $s_4^{\mathrm{Au}}(\omega)$ are the fourth-order demodulated harmonics of the near-field amplitude detected for hBN and Au standard reference sample, respectively. All nano-IR imaging experiments were conducted at ambient atmosphere.

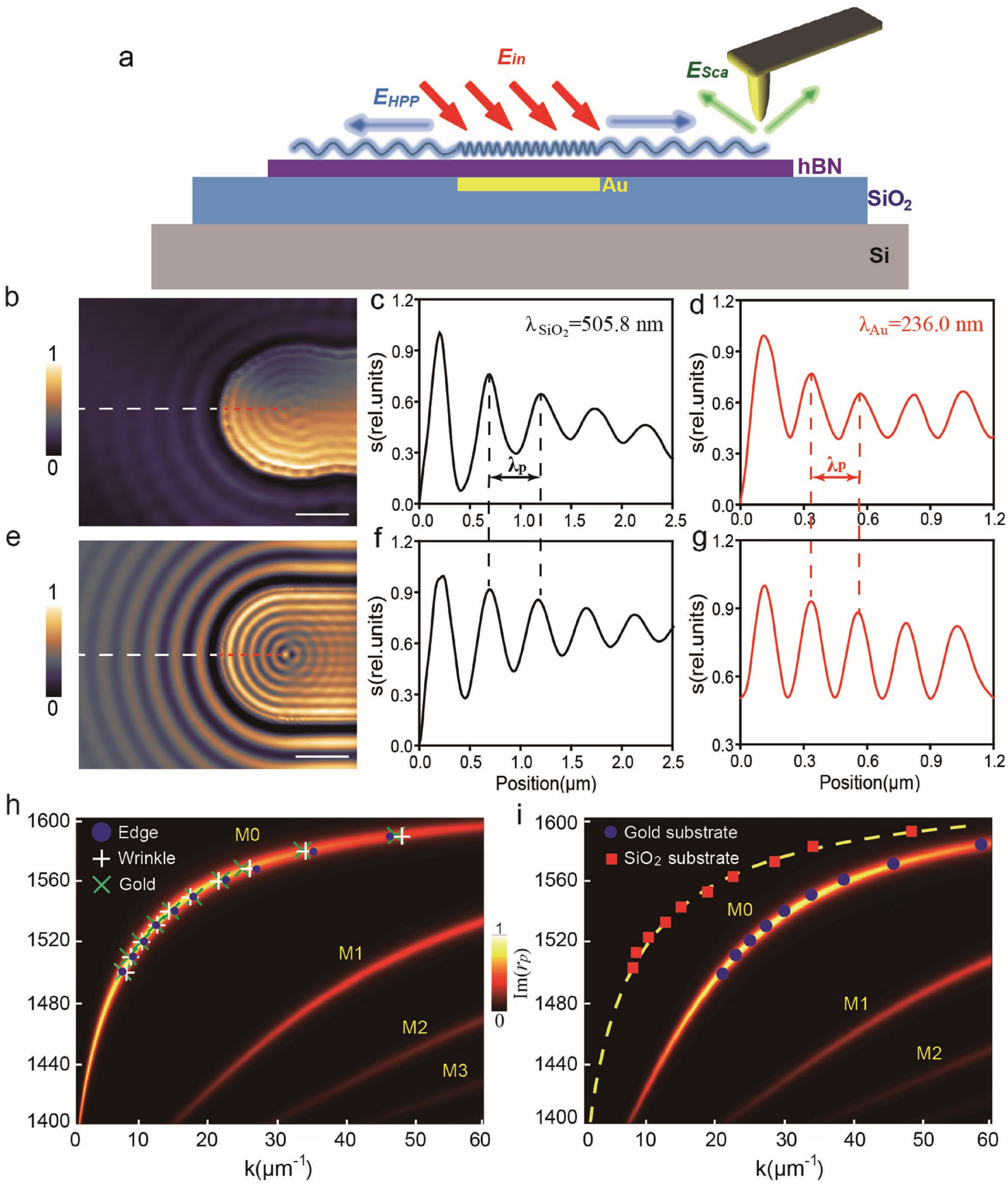

Figure 4. Verification of the compression of type 2 HPPs in the hBN crystal. a) Illustration of the experiment. The gold nanoantenna is encapsulated between hBN and SiO_2 substrate. The same hBN sample measured in Figure 3 is transferred to cover the fabricated gold antenna. b) Experimental images illustrating the near-field distribution around the gold antenna for ω_0 = 1530 cm^{-1}. c,d) The line profiles along the dashed white (on SiO_2 substrate) and red (on gold substrate) line in (b), respectively. The wavelength of propagating HPPs is compressed about twice on gold substrate. e) Corresponding numerical simulation of near-field distribution shown in (b). f,g) The line profiles along the dashed white and red line in (e), respectively. h) The dispersion relation of HPPs in 77 nm hBN slab. The white and green crosses indicate data from wrinkle-launched and gold-launched HPPs, respectively. The dots are data extracted from classical tip-launched HPPs at edge of the same hBN crystal and the background color shows the imaginary part of the Fresnel reflection coefficient. The wavelengths measured at hBN edge were stretched by a factor of two to account for the interference of standing wave. i) Experimental dispersion relation of HPPs in hBN crystal on top of dielectric substrate (red squares) and gold substrate (blue dots), respectively. The corresponding theoretical results are also presented as yellow dashed line and a false-color map. Scale bar, 1 μm.

Theoretical Calculation of the Dispersion Diagrams: In order to get the dispersion of phonon polariton in hBN, the complex reflectivity $r_p(q,\omega)$ containing the information of HPPs was calculated, considering a three layer structure system: air, hBN, and substrate. The interface reflectivity r_a and r_s from hBN to air, and hBN to substrate can be derived from the Fresnel equations. Further, taking into account the multireflection between these two interfaces, the reflectivity of the interface from air to the hBN layer r_p can be expressed as

$$r_a = \frac{\varepsilon^{\perp} k_a^z - \varepsilon_a k_e^z}{\varepsilon^{\perp} k_a^z + \varepsilon_a k_e^z} \tag{4}$$

$$r_s = \frac{\varepsilon_s k_e^z - \varepsilon^{\perp} k_s^z}{\varepsilon_s k_e^z + \varepsilon^{\perp} k_s^z} \tag{5}$$

$$r_p = \frac{r_a + r_s e^{i2k_e^z d}}{1 + r_a r_s e^{i2k_e^z d}} \tag{6}$$

Where, ε_a, $\varepsilon^{\perp}$, and ε_s refer to the permittivity of air, hBN (the out-of-plane component), and substrate, respectively. k_a^z or k_s^z represents the *z*-axis component momentum of the photon in air or substrate, the momentum $k_e^z = \sqrt{\varepsilon^{\perp}(\omega/c)^2 - \frac{\varepsilon^{\perp}}{\varepsilon^{\parallel}} q^2}$ corresponding an "extraordinary ray" of hBN due to a uniaxial anisotropy property. The *d* represents the thickness of hBN crystal.

Numerical Simulations: All numerical simulations in this work were conducted by the commercial software package Comsol in 3D Wave Optics Module, which is based on finite boundary element method. Since the AFM tip just acted as a passive scatter, a plane-wave illumination was set as the excitation resource through background scattering field. The mesh types and sizes were optimized to ensure a good convergence of simulated results. In all simulations, the absolute values of electric field over 60 nm above the samples and corresponding averaged line profiles were recorded.

Supporting Information

Supporting Information is available from the Wiley Online Library or from the author.

Acknowledgements

This work was supported by the National Key Research and Development Program of China (2016YFA0203500), the National Natural Science Foundation of China (Grant No.11474350), the National Basic Research Program of China (Nos.' 2013CB922200 & 2012YQ1200470403 to Z.S.), the National Basic Research Program of China (No. 2014CB921001), the Key Research Program of Frontier Sciences, CAS (No. QYZDJSSW-SLH020), the Strategic Priority Research Program (B) of the Chinese Academy of Sciences (No. XDB07030200), the State Key Laboratory of Optoelectronic Materials and Technologies (Sun Yat-sen University), and the State Key Laboratory for Artificial Microstructure and Mesoscopic Physics (Peking University).

Conflict of Interest

The authors declare no conflict of interest.

Keywords

dielectric environments, dispersion, hexagonal boron nitride, hyperbolic phonon polaritons, wrinkles

Received: May 4, 2017
Revised: July 13, 2017
Published online:

[1] D. N. Basov, M. M. Fogler, F. J. Garcia de Abajo, *Science* **2016**, *6309*, 354.
[2] T. Low, A. Chaves, J. D. Caldwell, A. Kumar, N. X. Fang, P. Avouris, T. F. Heinz, F. Guinea, L. Martin-Moreno, F. Koppens, *Nat. Mater.* **2017**, *16*, 182.
[3] G. X. Ni, H. Wang, J. S. Wu, Z. Fei, M. D. Goldflam, F. Keilmann, B. Ozyilmaz, A. H. Castro Neto, X. M. Xie, M. M. Fogler, D. N. Basov, *Nat. Mater.* **2015**, *14*, 1217.
[4] L. Ju, Z. Shi, N. Nair, Y. Lv, C. Jin, J. Velasco, C. Ojedaaristizabal, H. A. Bechtel, M. C. Martin, A. Zettl, *Nature* **2015**, *520*, 650.
[5] L. Jiang, Z. Shi, B. Zeng, S. Wang, J. Kang, T. Joshi, C. Jin, L. Ju, J. Kim, T. Lyu, *Nat. Mater.* **2016**, *15*, 840.
[6] S. Biehs, M. Tschikin, P. Benabdallah, *Phys. Rev. Lett.* **2012**, *109*, 104301.
[7] Z. Liu, H. Lee, Y. Xiong, C. Sun, X. Zhang, *Science* **2007**, *315*, 1686.
[8] J. Chen, M. Badioli, P. Alonsogonzalez, S. Thongrattanasiri, F. Huth, J. Osmond, M. Spasenovic, A. Centeno, A. Pesquera, P. Godignon, *Nature* **2012**, *487*, 77.
[9] Z. Fei, A. S. Rodin, G. O. Andreev, W. Bao, A. S. Mcleod, M. Wagner, L. Zhang, Z. Zhao, M. H. Thiemens, G. Dominguez, *Nature* **2012**, *487*, 82.
[10] A. Woessner, M. B. Lundeberg, Y. Gao, A. Principi, P. Alonsogonzalez, M. Carrega, K. Watanabe, T. Taniguchi, G. Vignale, M. Polini, *Nat. Mater.* **2015**, *14*, 421.
[11] S. Dai, Q. Ma, M. Liu, T. Andersen, Z. Fei, M. Goldflam, M. Wagner, K. Watanabe, T. Taniguchi, M. H. Thiemens, *Nat. Nanotechnol.* **2015**, *10*, 682.
[12] J. D. Caldwell, A. V. Kretinin, Y. Chen, V. Giannini, M. M. Fogler, Y. Francescato, C. T. Ellis, J. G. Tischler, C. R. Woods, A. J. Giles, M. Hong, K. Watanabe, T. Taniguchi, S. A. Maier, K. S. Novoselov, *Nat. Commun.* **2014**, *5*, 5221.
[13] S. Dai, Q. Ma, T. Andersen, A. S. McLeod, Z. Fei, M. K. Liu, M. Wagner, K. Watanabe, T. Taniguchi, M. Thiemens, F. Keilmann, P. Jarillo-Herrero, M. M. Fogler, D. N. Basov, *Nat. Commun.* **2015**, *6*, 6963.
[14] P. Li, M. Lewin, A. V. Kretinin, J. D. Caldwell, K. S. Novoselov, T. Taniguchi, K. Watanabe, F. Gaussmann, T. Taubner, *Nat. Commun.* **2015**, *6*, 7507.
[15] E. Yoxall, M. Schnell, A. Y. Nikitin, O. Txoperena, A. Woessner, M. B. Lundeberg, F. Casanova, L. E. Hueso, F. H. L. Koppens, R. Hillenbrand, *Nat. Photonics* **2015**, *9*, 674.
[16] a) J. Yao, Z. Liu, Y. Liu, Y. Wang, C. Sun, G. Bartal, A. M. Stacy, X. Zhang, *Science* **2008**, *321*, 930; b) X. Yang, J. Yao, J. Rho, X. Yin, X. Zhang, *Nat. Photonics* **2012**, *6*, 450.
[17] A. J. Hoffman, L. Alekseyev, S. S. Howard, K. J. Franz, D. Wasserman, V. A. Podolskiy, E. E. Narimanov, D. L. Sivco, C. Gmachl, *Nat. Mater.* **2007**, *6*, 946.
[18] S. Dai, Z. Fei, Q. Ma, A. S. Rodin, M. Wagner, A. S. McLeod, M. K. Liu, W. Gannett, W. Regan, K. Watanabe, T. Taniguchi, M. Thiemens, G. Dominguez, A. H. Castro Neto, A. Zettl, F. Keilmann, P. Jarillo-Herrero, M. M. Fogler, D. N. Basov, *Science* **2014**, *343*, 1125.
[19] X. G. Xu, B. G. Ghamsari, J. H. Jiang, L. Gilburd, G. O. Andreev, C. Zhi, Y. Bando, D. Golberg, P. Berini, G. C. Walker, *Nat. Commun.* **2014**, *5*, 4782.
[20] J. Chen, M. L. Nesterov, A. Y. Nikitin, S. Thongrattanasiri, P. Alonsogonzalez, T. M. Slipchenko, F. Speck, M. Ostler, T. Seyller, I. Crassee, *Nano Lett.* **2013**, *13*, 6210.
[21] Z. Fei, A. S. Rodin, W. Gannett, S. Dai, W. Regan, M. Wagner, M. Liu, A. S. Mcleod, G. Dominguez, M. H. Thiemens, *Nat. Nanotechnol.* **2013**, *8*, 821.
[22] Z. Fei, G. O. Andreev, W. Bao, L. M. Zhang, A. S. Mcleod, C. Y. Wang, M. K. Stewart, Z. Zhao, G. Dominguez, M. H. Thiemens, *Nano Lett.* **2011**, *11*, 4701.

[23] A. Y. Nikitin, E. Yoxall, M. Schnell, S. Vélez, I. Dolado, P. Alonso-Gonzalez, F. Casanova, L. E. Hueso, R. Hillenbrand, *ACS Photonics* **2016**, *3*, 924.
[24] P. Alonso, A. Y. Nikitin, F. Golmar, A. Centeno, A. Pesquera, S. Velez, J. Chen, G. Navickaite, F. H. L. Koppens, A. Zurutuza, *Science* **2014**, *344*, 1369.
[25] Z. Shi, H. A. Bechtel, S. Berweger, Y. Sun, B. Zeng, C. Jin, H. Chang, M. C. Martin, M. B. Raschke, F. Wang, *ACS Photonics* **2015**, *2*, 790.
[26] Z. Fei, M. D. Goldflam, J. S. Wu, S. Dai, M. Wagner, A. S. McLeod, M. K. Liu, K. W. Post, S. Zhu, G. C. A. M. Janssen, M. M. Fogler, D. N. Basov, *Nano Lett.* **2015**, *15*, 8271.
[27] M. Wagner, Z. Fei, A. S. Mcleod, A. S. Rodin, W. Bao, E. G. Iwinski, Z. Zhao, M. Goldflam, M. Liu, G. Dominguez, *Nano Lett.* **2014**, *14*, 894.
[28] A. Y. Nikitin, P. Alonso, S. Velez, S. Mastel, A. Centeno, A. Pesquera, A. Zurutuza, F. Casanova, L. E. Hueso, F. H. L. Koppens, *Nat. Photonics* **2016**, *10*, 239.